ELSEVIER

International Journal of Solids and Structures 41 (2004) 1209–1234

INTERNATIONAL JOURNAL OF SOLIDS and STRUCTURES

www.elsevier.com/locate/ijsolstr

Nonlinear thermomechanical oscillations of shape-memory devices

W. Lacarbonara *, D. Bernardini, F. Vestroni

Dipartimento di Ingegneria Strutturale e Geotecnica, University of Rome La Sapienza, via Eudossiana 18, Rome 00184, Italy

Received 10 October 2003; received in revised form 10 October 2003

Abstract

The nonlinear responses and bifurcations of shape-memory oscillators, based on a thermomechanical model, are investigated employing a numerically refined approach. Because of the discontinuities of the system tangent stiffness, classical gradient-based shooting-type techniques for calculating the periodic responses are not applicable. These solutions are then sought as the fixed points of the Poincaré map combined with a path-following procedure. The Jacobian of the map is calculated via a central finite-difference scheme and its eigenvalues, the Floquet multipliers, are computed to ascertain the stability of the solutions and the codimension-one bifurcations. Frequency–response curves are constructed for shape-memory oscillators characterized by different hysteresis loops and for various excitation levels. The investigations are conducted both in *isothermal* and *nonisothermal* conditions and the main outcomes are comparatively discussed. A rich class of solutions and bifurcations—including jump phenomena, pitchfork, period-doubling, Hopf bifurcations, complete bubble structures culminating into chaos—is found; quasiperiodic motions arise in nearly adiabatic conditions.

Keywords: Shape-memory alloys; Hysteresis; Thermomechanical coupling; Quasiperiodicity; Hopf bifurcation; Period-doubling cascade; Chaos

1. Introduction

In recent years, the applications based on shape-memory materials (SMM) are receiving increasing attention and, presently, they also include devices tailored for the reduction of structural vibrations (Saadat et al., 2002). The technically useful features of SMM's are being exploited to engineer devices possessing energy dissipation capabilities without residual displacements after unloading and with great reliability of performance over time due to the high fatigue resistance (Clark et al., 1995).

Because in the majority of technical applications, SMM's are subjected to quasistatic actions, the material behavior under slow loads was extensively studied both from a theoretical and a practical point of view. On the other hand, when SMM's are subjected to relatively fast time-varying loads, as in the case of

* Corresponding author. Tel.: +39 06 44585293; fax: +39 06 4884852.
E-mail address: walter.lacarbonara@uniromal.it (W. Lacarbonara).

0020-7683/$ - see front matter © 2003 Elsevier Ltd. All rights reserved.
doi:10.1016/j.ijsolstr.2003.10.015

dynamic actuators, the thermodynamical interactions with the environment become appreciable and need to be carefully considered.

More specifically, since SMM's exhibit hysteretic behavior with a strong coupling between thermal and mechanical variables, the dynamical system to be studied is a thermomechanical hysteretic oscillator. The associated response is described by the displacement, the velocity, an internal variable quantifying the phase transformations, and also by the temperature. The evolution of the temperature is governed by an independent balance equation obtained from the laws of thermodynamics.

Pseudoelasticity in SMM's is the consequence of solid phase transformations between Austenite (A) and multiple variants of Martensite (M). The application of a mechanical load can induce an exothermic transformation $(A \rightarrow M)$ that gives rise to a plateau in the stress–strain plane. Thereafter, the subsequent release of the load causes the reverse $(M \rightarrow A)$ endothermic transformation and produces a hysteresis loop (Otsuka and Shimizu, 1986). The heat released and absorbed during the phase transformations is partly exchanged with the surrounding environment and partly modifies the temperature of the SMM. The magnitude of these temperature variations increases with the loading rate (see Fig. 1) and affects significantly the mechanical response thereby becoming a critical issue in the application design. Therefore, when the material is used under dynamic conditions, temperature variations need to be taken into account in the modeling and knowledge of the nonlinear thermomechanical behavior becomes necessary and preliminary for design purposes.

Feng and Li (1996) and Thomson et al. (1995) addressed some aspects of the response of pseudoelastic oscillators, mainly by means of direct numerical integration, on the basis of constitutive models which neglect thermal aspects by assuming a constant temperature. Oberaigner et al. (1995) used a more refined constitutive model; however, they studied only a few aspects of the dynamic response. A nonlinear dynamic characterization of the thermomechanical responses of pseudoelastic oscillators was presented in Vestroni and Bernardini (1999) where a multi-harmonic balance method and a simple multi-linear thermodynamical model for the SMM were used. Later, in Bernardini and Vestroni (2000), the thermomechanical model developed by Ivshin and Pence (1994) was extended so as to be directly applicable for the description of the restoring force in dynamical systems. Employing a multi-harmonic balance method, this model was used to investigate the thermomechanical nonlinear responses in Bernardini and Vestroni (2003).

In the present work, nonlinear dynamic investigations of both isothermal and nonisothermal pseudoelastic one-degree-of-freedom oscillators, governed by the above mentioned constitutive model, are performed employing a numerically accurate approach. The methodology is based on the use of the Poincaré map (along with a finite-difference evaluation of its Jacobian) to determine the periodic responses to harmonic excitations and the associated codimension-one bifurcations. The basic algorithm was developed in Lacarbonara et al. (1999), later used in Lacarbonara et al. (2001) and Lacarbonara and Vestroni (2003), to circumvent the difficulties associated with the nondifferentiable nature of the governing vector field in

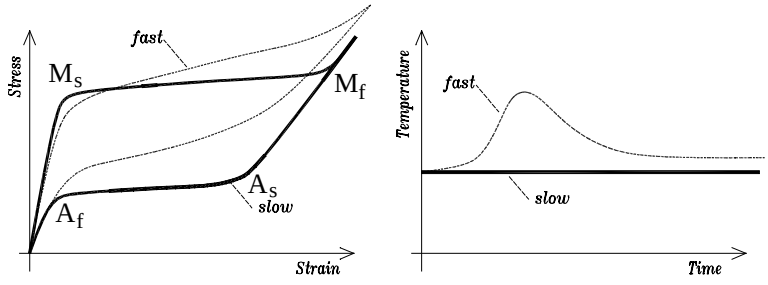

Fig. 1. Schematic isothermal and nonisothermal pseudoelasticity with the start and finish of the phase transformations: A → M (points M_s; M_f) and M → A (points A_s; A_f).

hysteretic (and more general nonsmooth) systems. The use of the Poincaré map method in the time domain saves also computational efforts compared to multi-harmonic balance methods since the Jacobian of the map, used as basis for the predictor in the path-following scheme, corresponds to the system monodromy matrix whose eigenvalues, the Floquet multipliers, govern the stability of the solutions.

In the isothermal case, the dynamical system is three-dimensional as the state space is described by the displacement x, the velocity v, and the internal variable ξ which governs the evolution of the phase transformations that occur in the SMM. In the nonisothermal case, the state space becomes four-dimensional as the temperature ϑ is added to x, v, and ξ in the state-space description.

Frequency–response curves for the displacement and temperature are computed and the stability analysis is concurrently carried out. Rich nonlinear dynamic scenarios are found in the range of material parameters that correspond to technical vibration reduction devices. The influence of the thermal aspects and the material parameters such as the width of the hysteresis loops and the slopes of the pseudoelastic plateaus on the dynamic behavior are also discussed. The differences in the thermomechanical behaviors arising from isothermal and nonisothermal regimes are clarified.

2. The thermomechanical model of shape-memory devices

The dynamical system in Fig. 2 is a pseudoelastic oscillator of mass m embedded in a convective environment at temperature ϑ_E and excited by a harmonic force, $F(t) = \gamma \cos \Omega t$. The restoring force is provided by a pseudoelastic device (f) and a linear viscous dashpot with damping coefficient μ. During oscillations, the mass and the dashpot remain at the constant temperature ϑ_E whereas the temperature ϑ of the pseudoelastic device may change.

A pseudoelastic device is a proper arrangement of SMM components (e.g., wires or bars) connecting two points that can undergo a relative displacement x. The thermomechanical formulation for the modeling of the device here presented is based on the work by Ivshin and Pence (1994), further elaborated in Bernardini and Vestroni (2000). Since the peculiar response of SMM's is determined by the Austenite–Martensite phase transformations, the fraction $\xi \in [0, 1]$ of one of the two phases, namely Martensite, is introduced as the *internal variable* in order to describe the evolution of the phase transformations. Therefore, when the device is in a fully austenitic state (A), $\xi = 0$, whereas, when it is in a fully martensitic state (M), $\xi = 1$. An important feature is that a length increase is observed when ξ increases ($A \to M$ forward transformation) and vice versa. This effect is inherent in the material microstructure and is taken into account in the model by the material parameter δ defined as $x_{(\xi=1)} - x_{(\xi=0)} =: \delta$ with $\delta > 0$ representing the maximum transformation displacement.

The set of equations governing the response of the thermomechanical system is given by

$$m\ddot{x} = \gamma \cos \Omega t - f - \mu \dot{x} \tag{1}$$

$$\dot{e} = f\dot{x} + \dot{Q} \tag{2}$$

$$\vartheta \dot{\eta} = \dot{Q} + \dot{\Gamma} \tag{3}$$

$$\dot{\Gamma} \geqslant 0 \tag{4}$$

where the dot denotes differentiation with respect to time, e indicates the internal energy, $\dot{Q}$ is the rate of heat exchange with the environment, $\dot{\Gamma}$ the rate of energy dissipation, ϑ the temperature of the device and η its entropy. Eq. (1) is the balance law of linear momentum, whereas the others express the first and the second law of thermodynamics. Specifically, Eq. (2) represents the internal energy balance (first law), whereas Eqs. (3) and (4) are the balance of entropy and Clausius–Duhem inequality (second law),

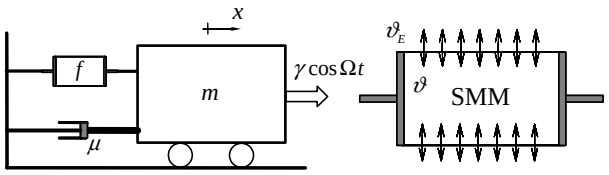

Fig. 2. A scheme of the shape-memory oscillator.

respectively. The inequality (4) and the internal energy balance (2) will be used to enforce a constraint on the constitutive assumptions as it will be shown further on. The other two equations, namely (1) and (3), will then remain as the equations governing the system dynamics. Because it is more convenient to use the free energy function $\Phi = e - \vartheta\eta$ instead of the internal energy e, the first law of thermodynamics (2) is rewritten, using Eq. (3), in the form

$$\dot{\Phi} = f\dot{x} - \eta\dot{\vartheta} - \dot{\Gamma} \tag{5}$$

In the above equations, the unknown functions are eight, namely, x, ϑ, ξ, f, Φ, η, $\dot{Q}$ and $\dot{\Gamma}$ while the balance equations are three. Consequently, five constitutive equations are needed and, hereafter, will be specified through expressions for f, η, Φ, $\dot{\xi}$ and $\dot{Q}$.

The equation for $\dot{Q}$ describes the heat exchange between the device and the environment. It is assumed that such an exchange takes place primarily by convection, which can be reasonably modeled by Newton's heating law

$$\dot{Q} = h(\vartheta_{\mathrm{E}} - \vartheta) \tag{6}$$

where $h \geqslant 0$ is the heat exchange coefficient.

Using the first law in the form (5) and the Clausius–Duhem inequality (4) leads to

$$f = \frac{\partial\Phi}{\partial x}, \quad \eta = -\frac{\partial\Phi}{\partial\vartheta}, \quad \dot{\Gamma} = \Pi\dot{\xi} \geqslant 0 \tag{7}$$

where $\Pi = -\partial\Phi/\partial\xi$ is the thermodynamic force (driving force) conjugated with the rate of phase transformation $\dot{\xi}$. Taking into account the equalities and restrictions (7), it turns out that only two constitutive equations for Φ and $\dot{\xi}$ are needed to completely specify the model, as it is typical in the framework of thermodynamics with internal variables (Coleman and Gurtin, 1967).

The following free energy function has been used to model the device (Bernardini, 2001)

$$\Phi = \frac{K}{2}(x - \mathrm{sgn}(x)\delta\xi)^2 + c\left(\vartheta - \vartheta_0 - \vartheta\ln\frac{\vartheta}{\vartheta_0}\right) + (\vartheta - \vartheta_0)b\delta\xi + a_0 - b_0\vartheta, \tag{8}$$

where $K > 0$ is the elastic stiffness, $c > 0$ is the heat capacity, $b > 0$ is the slope in the temperature transformation–force plane, a_0 and b_0 are the internal energy and entropy of the device in the fully austenitic state at the reference temperature ϑ_0, respectively. The constitutive equations for the restoring force, entropy and thermodynamic driving force directly follow from (7) as

$$f = K(x - \mathrm{sgn}(x)\delta\xi) \tag{9}$$

$$\eta = c\ln\frac{\vartheta}{\vartheta_0} - b\delta\xi + b_0 \tag{10}$$

$$\Pi = K\delta(|x| - \delta\xi) - b\delta(\vartheta - \vartheta_0) \tag{11}$$

In the restoring force (9), $\mathrm{sgn}(x)\delta\xi$ is the pseudoelastic part of the total displacement and the signum function has been introduced to reproduce a symmetric response that is typical in practical devices (although the material itself commonly exhibits asymmetry under tension and compression).

The constitutive equation for $\dot{\xi}$ is known as the *transformation kinetic* since it describes the evolution of the phase transformations. It is prescribed in the form

$$\dot{\xi} = G(\Pi, \xi, \mathrm{sgn}(\dot{\xi}))\dot{\Pi} \tag{12}$$

with the hysteresis operator

$$G = \begin{cases} k_1(1-\xi)[1+\tanh(k_1\Pi + k_2)], & \text{if } \dot{\xi} > 0 \\ k_3\xi[1-\tanh(k_3\Pi + k_4)], & \text{if } \dot{\xi} < 0 \end{cases} \tag{13}$$

Clearly, the operator G, taking into account (11), depends on the state. This leads to a modified version of the Ivshin-Pence model. The hysteresis loops obtained with this model were shown to be in good agreement with the experimental results as reported in Bernardini and Pence (2002).

The function G takes different forms for increasing or decreasing ξ in order to describe the $A \to M$ and $M \to A$ transformations. The material parameters k_i can be identified from experimental data as explained below. The transformation kinetic can be integrated, separately for each transformation, to give the relation between the phase fraction ξ and the driving force Π in closed form. These expressions are given, for the forward and reverse transformations, respectively, by

$$\xi = \frac{1}{2} + \frac{1}{2}\tanh(k_1\Pi + k_2), \quad \xi = \frac{1}{2} + \frac{1}{2}\tanh(k_3\Pi + k_4)$$

The hyperbolic tangent function has a characteristic sigmoidal shape (Fig. 3) which provides a good approximation of the experimental measurements of the phase fraction evolution. The actual shape of the phase fraction evolution is regulated by k_1 (k_3 for the reverse transformation), that governs the slope of the transformation, and by k_2 (k_4 for the reverse transformation) that regulates the actual values of Π at which the transformation takes place (by shifting the curve to the left or to the right). As mentioned, Eq. (11) then provides the key to translate the evolution of ξ in terms of Π into the corresponding evolution in terms of the displacement and temperature; that is,

$$\dot{\xi} := -\frac{Gb\delta}{1 + K\delta^2 G}\left(\dot{\vartheta} - \mathrm{sgn}(x)\frac{K}{b}\dot{x}\right) \tag{14}$$

Moreover, accounting for Eq. (13) and the fact that k_1 and $k_3 > 0$, it is $G > 0$; hence, the denominator in the transformation kinetic never vanishes.

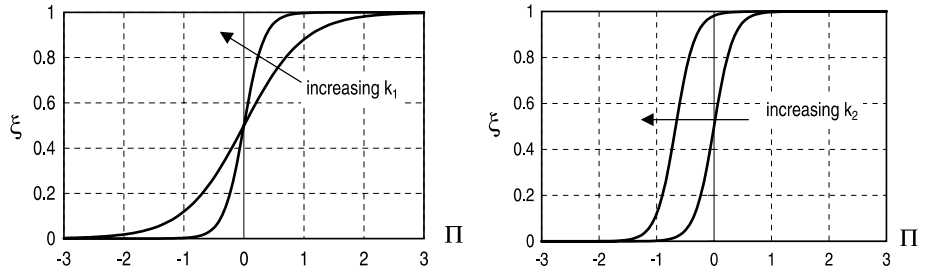

Fig. 3. Effect of the parameters k_1 and k_2 on the evolution of ξ in terms of Π for the forward A → M transformation. Analogous effect is provided by k_3 and k_4 on the evolution for the reverse M → A transformation.

In order to show how the kinetic affects the force–displacement behavior, the simplest loading case is considered: a quasistatic force $F(t)$ at constant temperature $\vartheta(t) = T$. Taking into account that the driving force can also be written as a function of F, $\Pi = \delta|F| - b\delta(\vartheta - \vartheta_0)$, the actual evolution of ξ under loading (forward transformation) can be computed and then substituted into $Kx = F + K\delta\xi$ yielding the closed-form expression of the force–displacement loading curve as

$$x = \frac{F}{K} + \frac{\delta}{2}(1 + \tanh(|F|k_1\delta + k_2))$$

Considering the hyperbolic tangent curves obtained for the forward and reverse transformations, the typical shapes of pseudoelastic hysteresis loops are obtained; examples of actual hysteresis loops predicted by the model are given in the next sections.

Finally, the identification of the parameters k_1 and k_2 from force–displacement experimental curves at constant temperature T is discussed. The forces, f_{Ms} and f_{Mf}, at which the forward transformation starts and finishes, respectively, are experimentally measurable quantities. The k's can be identified by setting

$$\xi_{\mathrm{r}} = \frac{1}{2} + \frac{1}{2}\tanh(k_1\delta f_{\mathrm{Ms}} - b\delta k_1(T - \vartheta_0) + k_2)$$

$$1 - \xi_{\mathrm{r}} = \frac{1}{2} + \frac{1}{2}\tanh(k_1\delta f_{\mathrm{Mf}} - b\delta k_1(T - \vartheta_0) + k_2)$$

where ξ_{r} is the residual Martensite at the conventional start of the transformation. Introducing, for convenience, $r := \tanh^{-1}(1 - 2\xi_{\mathrm{r}})$ yields

$$k_1 = \frac{-2r}{\delta(f_{\mathrm{Ms}} - f_{\mathrm{Mf}})}, \quad k_2 = r - 2r\frac{b(T - \vartheta_0) - f_{\mathrm{Mf}}}{f_{\mathrm{Ms}} - f_{\mathrm{Mf}}}$$

The parameter ξ_{r} then regulates the smoothness of the transition around f_{Ms} and f_{Mf}. The greater ξ_{r}, the smoother the transition is. The case of reverse transformation provides similar expressions for k_3 and k_4.

After substitution of the constitutive equation for f, η, $\dot{\Gamma}$, and $\dot{Q}$, the final governing equations are the balance of linear momentum (1), the balance of entropy (3), and the transformation kinetic (14). This gives a set of three ordinary-differential equations in the unknown functions $x(t)$, $\vartheta(t)$, $\xi(t)$ which can be rearranged in normal form as a set of four first-order equations in $\mathbf{x} = [x, v, \xi, \vartheta]^{\top}$; that is,

$$\dot{\widehat{x}} = \widehat{v} \tag{15}$$

$$\dot{\widehat{v}} = \widehat{\gamma}\cos\widehat{\Omega}\hat{t} - (\widehat{x} - \mathrm{sgn}(\widehat{x})\lambda\xi) - 2\zeta\widehat{v} \tag{16}$$

$$\dot{\xi} = \frac{Z_1}{Z_1Z_2 - 1}[\mathrm{sgn}(\widehat{x})J\widehat{v} - \widehat{h}(\widehat{\vartheta} - \widehat{\vartheta}_{\mathrm{E}})] \tag{17}$$

$$\dot{\widehat{\vartheta}} = \frac{1}{1 - Z_1Z_2}[\mathrm{sgn}(\widehat{x})JZ_1Z_2\widehat{v} - \widehat{h}(\widehat{\vartheta} - \widehat{\vartheta}_{\mathrm{E}})] \tag{18}$$

where the hat denotes nondimensional variables

$$\begin{aligned} &\hat{t} = \omega t, \quad \widehat{x} = \frac{x}{x_{\mathrm{Ms}}}, \quad \widehat{\vartheta} = \frac{\vartheta}{\vartheta_{\mathrm{r}}} \\ &\widehat{G} = Gb\delta\vartheta_{\mathrm{r}}, \quad Z_1 = \frac{\widehat{G}}{1 + J\lambda\widehat{G}}, \quad Z_2 = -L[J(|\widehat{x}| - \lambda\xi) + \widehat{\vartheta_0}] \end{aligned} \tag{19}$$

with $\omega^2 = K/m$ and the nondimensional parameters are

$$\lambda = \frac{\delta}{x_{\mathrm{Ms}}}, \quad L = \frac{b\delta}{c}, \quad \widehat{h} = \frac{h}{c\omega}, \quad J = \frac{f_{\mathrm{Ms}}}{b\vartheta_{\mathrm{r}}}, \quad \hat{k}_j = k_j b\delta\vartheta_r, \quad j = 1,3$$
$$\zeta = \frac{\mu}{2\omega m}, \quad \widehat{\gamma} = \frac{\gamma}{f_{\mathrm{Ms}}}, \quad \widehat{\Omega} = \frac{\Omega}{\omega} \tag{20}$$

Since the kinetic parameters $\hat{k}_i$ do not possess a direct physical meaning, they can be suitably expressed in terms of new parameters, $\widehat{q}_i$, allowing, conversely, for a more direct physical interpretation. These parameters are conveniently defined as

$$\widehat{q}_1 = \frac{f_{\mathrm{Mf}}}{f_{\mathrm{Ms}}}, \quad \widehat{q}_2 = \frac{f_{\mathrm{Af}}}{f_{\mathrm{As}}}, \quad \widehat{q}_3 = \frac{f_{\mathrm{As}}}{f_{\mathrm{Ms}}}$$

where f_{Ms}, f_{Mf}, f_{As}, and f_{Af} are the forces at the start and finish of the associated transformations at the reference temperature ϑ_{r}. The relations between the $\hat{k}'$s and $\widehat{q}'$s are

$$\hat{k}_1 = \frac{2r}{J(\widehat{q}_1 - 1)}, \quad \hat{k}_2 = \frac{2(1-\vartheta_0) - J(\widehat{q}_1 + 1)}{J(\widehat{q}_1 - 1)} r$$
$$\hat{k}_3 = \frac{2r}{(1-\widehat{q}_2)\widehat{q}_3 J}, \quad \hat{k}_4 = \frac{2(1-\vartheta_0) - \widehat{q}_3 J(1+\widehat{q}_2)}{(1-\widehat{q}_2)\widehat{q}_3 J} r$$

In order to obtain upper and lower pseudoelastic plateaus with the same force variation, the condition $f_{\mathrm{Mf}} - f_{\mathrm{Ms}} = f_{\mathrm{As}} - f_{\mathrm{Af}}$ is enforced. This results into a constraint on $\widehat{q}_2$ in the form $\widehat{q}_2 = (1 + \widehat{q}_3 - \widehat{q}_1)/\widehat{q}_3$. Moreover, according to a common practice in the materials science literature, the equilibrium temperature $\widehat{\vartheta}_0$ can be expressed as a mean value of the force-free transformation temperatures; that is, $\widehat{\vartheta}_0 = 1 - J(1 + \widehat{q}_1 + \widehat{q}_3 + \widehat{q}_2\widehat{q}_3)/4$.

Henceforth, only nondimensional variables and parameters will be considered and the hat will be omitted for ease of notation.

3. Responses and bifurcations: a numerically accurate approach

The objective of the investigations is a detailed study of the nonlinear responses and their bifurcations in shape-memory oscillators both in isothermal and nonisothermal conditions. The study is directed to outline the expected, yet not sufficiently investigated, differences in the dynamical behaviors when shape-memory devices operate in isothermal conditions in contrast with nonisothermal conditions. This is accomplished by constructing frequency–response curves for different material parameters and various excitation amplitudes and by monitoring the paths of the Floquet multipliers to assess the response stability and bifurcations.

When the detected bifurcations lead to new attractors, the post-bifurcation scenarios are investigated with either the path-following procedure or via direct numerical integration of the governing equations. In these investigations, the employed strategy seeks to single out, among different shape-memory devices, those that, in isothermal conditions, exhibit complex dynamics. Subsequently, an in-depth investigation of these devices in nonisothermal regimes is carried out so as to outline the effects of the thermodynamical coupling.

The path-following procedure is based on the use of the Poincaré map for constructing the periodic solutions combined with arclength parameterization (Lacarbonara et al., 2001; Lacarbonara and Vestroni, 2003) upon variation of the selected control parameter, here the external frequency Ω.

When the device is harmonically excited by a T-periodic external force, for fixed Ω, the solution of Eqs. (15)–(18) can be written as $\mathbf{x} = \mathbf{x}(t, \mathbf{x}_0; \Omega)$ where $\mathbf{x}_0$ denotes the state vector at $t = t_0$. A Poincaré map, based on the return time $T_n = nT$, (i.e., $\mathbf{P}_n[\mathbf{z}; \Omega] : \mathbf{z} \to \mathbf{x}(T_n, \mathbf{z}; \Omega)$), is defined; then, a periodic solution can be sought as the fixed point of the map, that is, $\mathbf{P}_n[\mathbf{z}; \Omega] - \mathbf{z} = \mathbf{0}$. The Jacobian of the map, namely

$D_{\mathbf{z}}\mathbf{P}_n = \partial\mathbf{P}_n[\mathbf{z};\Omega]/\partial\mathbf{z}$, and the derivative of the map with respect to the control parameter, $d_{\Omega}\mathbf{P}_n = \partial\mathbf{P}_n[\mathbf{z};\Omega]/\partial\Omega$, are computed numerically via a finite-difference scheme.

The arclength s is used as the continuation parameter. To proceed to the neighboring solution on the branch at $s + \Delta s$, a Newton–Raphson scheme, based on a tangent predictor and combined with the bordering algorithm, is implemented. The iterations are continued until a convergence criterion is satisfied in the Newton–Raphson iterative scheme. Thereafter, the procedure furnishes the Jacobian matrix evaluated at the periodic solution (i.e., the monodromy matrix $\mathbf{\Phi}$); that is, $\mathbf{\Phi} = D_{\mathbf{z}}\mathbf{P}_n[\mathbf{z};\Omega]$. The eigenvalues of $\mathbf{\Phi}$, the Floquet multipliers, allow to ascertain the stability of the calculated orbit and its bifurcations.

A central-difference scheme was used for computing the Jacobian of the Poincaré map with $\delta_1 = \delta_2 = 10^{-3}$, $\epsilon_1 = \epsilon_2 = 10^{-6}$, and $\Delta t/T = 1/2048$ where δ_i and ϵ_i denote, respectively, the finite differences in the computation of $D_{\mathbf{z}}\mathbf{P}_n$ ($d_{\Omega}\mathbf{P}_n$) and the prescribed tolerances for the convergence test. Finally, $\Delta t/T$ indicates the time step normalized with respect to the excitation period in the integration scheme.

4. Isothermal regime

The first investigation deals with the isothermal case; because $\dot{\vartheta} = 0$, using Eq. (18), the heat exchange rate with the environment is given by $\dot{Q} = -JZ_1Z_2\mathrm{sgn}(x)\dot{x}$. Furthermore, substituting the obtained expression for $\dot{Q}$ into (17) yields

$$\dot{\xi} = -JZ_1\mathrm{sgn}(x)\dot{x} \tag{21}$$

Therefore, ϑ is excluded from the state-variable vector and the evolution of the 3D-vector field is governed by Eqs. (15), (16) and (21).

To construct the frequency–response curves, the nondimensional frequency Ω is used as the control parameter, the linear viscous damping coefficient is set to $\zeta = 0.05$ in all of the analyses, whereas the external excitation varies from low- to medium/high-amplitude levels γ, namely from 0.1 to 0.8 (i.e., 10–80% of the transformation force for the activation of the $\mathrm{A} \to \mathrm{M}$ phase transformation at the reference temperature).

According to the discussion in Section 2, in isothermal conditions, the independent material parameters are q_1, q_3, λ, and ξ_{r}. Because λ and ξ_{r} do not vary appreciably in engineering applications, they are set to typical values, 7.0 and 0.20, respectively.

In Fig. 4, the frequency–response curves obtained for various excitation levels are shown by setting the other material parameters q_1 and q_3 to 1.30 and 0.90, respectively. The restoring force–displacement loops

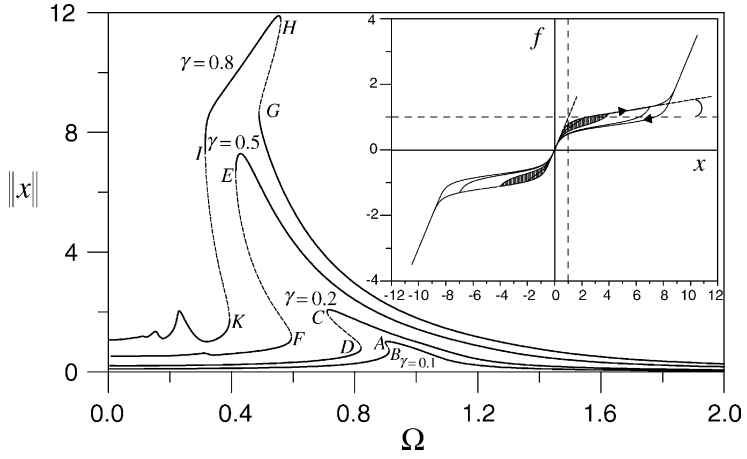

Fig. 4. Frequency–response curves in isothermal conditions when $q_1 = 1.30$ and $q_3 = 0.90$.

for different oscillation amplitudes are also shown; they are typical of practical shape-memory materials with a nonflat pseudoelastic plateau (presence of post-elastic stiffness). In these figures, and henceforth, $\|x\|$ indicates the maximum value of the displacement attained over one excitation cycle, continuous (dashed) lines denote stable (unstable) solutions.

The frequency–response curves are, as expected, of the softening type thus implying a decrease of the frequency with the oscillation amplitude. When the excitation level is $\gamma = 0.1$, the frequency–response curve exhibits a relatively small multivalued range due to the saddle-node bifurcations at A and B. Increasing the excitation amplitude, the multivalued range first enlarges and, then, above a certain value (about 0.5), it becomes smaller indicating that the curvature of the backbone curve decreases with the amplitude.

For a relatively high excitation amplitude, namely $\gamma = 0.8$, the shape of the frequency–response curve undergoes a major change; after the initial softening, the upper part of the curve is bent to the right resulting in a hardening behavior, as also reported in Bernardini and Vestroni (2003). The change in bending of the backbone curve is achieved when the maximum displacement overcomes the threshold displacement where the phase transformation into Martensite has been completed, that is, when $x \geqslant x_{\mathrm{Mf}}$. Since the device is in a fully martensitic state, it behaves, for further amplitude increments, as a linear elastic device with the same original elastic stiffness. The positive stiffness jump occurring at $x = x_{\mathrm{Mf}}$ results, of course, into a hardening behavior. The number of saddle-node bifurcations increases, starting from G to H and I until reaching the lower saddle-node at K. Decreasing the frequency, stable and unstable solution branches alternate until the lower nonresonant branch is reached. At this excitation amplitude, also the superharmonic resonance of order one-third is activated with a clear stable resonant peak indicating that the threshold excitation amplitude for this resonance is within the range 0.5–0.8.

It is worth commenting that, except for the hardening branch, the obtained frequency–response curves show qualitative features similar to those of other types of hysteretic oscillators such as the elastoplastic, Masing and Bouc-Wen oscillators (Masri, 1975; Wong et al., 1994a,b; Capecchi and Vestroni, 1990; Vestroni and Capecchi, 1997; Lacarbonara and Vestroni, 2003).

Next, the effects of hysteresis on the responses and associated bifurcations are investigated. In particular, two limiting cases of nearly flat pseudoelastic plateaus ($q_1 = 1.05$) with two different thicknesses of the hysteresis loops are considered: (i) a high level ($q_3 = 0.30$) and (ii) a low level ($q_3 = 0.60$). The frequency–response curves for case (i) are shown in Fig. 5. The bifurcation pattern is somehow similar to that depicted

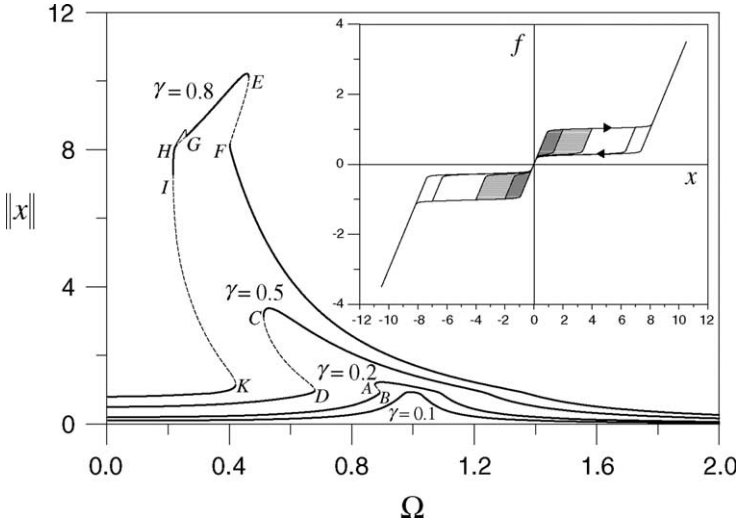

Fig. 5. Frequency–response curves in isothermal conditions when $q_1 = 1.05$ and $q_3 = 0.30$.

in Fig. 4, with a reduction of the oscillation amplitude as one would expect. In particular, when $\gamma = 0.1$, the frequency–response curve does not exhibit bifurcations whereas, for $\gamma = 0.2$ and $\gamma = 0.5$, two saddle-node bifurcations occur at A and B and C and D, respectively.

For a higher excitation amplitude, namely $\gamma = 0.8$, the frequency–response curve exhibits a greater number of bifurcations, apparently similar to that in Fig. 4. The first saddle-node bifurcation occurs at F and the second at E. Thereafter, decreasing the frequency along the upper resonant hardening branch, the symmetric solution becomes unstable at G via a pitchfork bifurcation (also known as symmetry-breaking) and, subsequently, it regains its stability at H by a reverse pitchfork bifurcation. The stable symmetric solution experiences saddle-node bifurcations at I and K. Exploring the post-bifurcation scenario following the pitchfork bifurcation at G, the stable nonsymmetric solution undergoes a period-doubling bifurcation thus giving rise to a period-doubled solution that disappears by a reverse period-doubling bifurcation.

Therefore, from the comparison between the nonflat with the nearly flat pseudoelastic plateau, it seems that the effects of the sharp decrease in the slope of the pseudoelastic plateau (compare the loops in Fig. 4 with those in Fig. 5) and the increased hysteretic dissipation are the following: (i) at low excitations, the periodic responses are globally stable, due to the higher dissipation; (ii) the oscillation amplitudes are generally reduced by the higher hysteresis; (iii) the threshold excitation level for the activation of the superharmonic resonances is greater; (iv) pitchfork bifurcations followed by period-doubling bifurcations occur on the upper (hardening) resonant branch.

The loss of symmetry of the solution at the pitchfork bifurcations and the subsequent period doubling of the nonsymmetric responses are likely due to the almost abrupt stiffness drop occurring at the beginning of the phase transformations. These instabilities are suffered by the system (Fig. 5) in spite of the increased hysteretic dissipation which, on the contrary, is usually expected to exert a stabilizing effect.

As mentioned, for devices with nearly flat plateaus, the case of relatively low hysteresis has also been investigated and the computed frequency–response curves are shown in Figs. 6 and 7. The bifurcation pattern is not significantly modified for low-to-medium excitation amplitudes; in general, the response amplitudes are higher than case (i) due to the reduced hysteresis. For a mid-range excitation amplitude, namely $\gamma = 0.6$, the resulting frequency–response curve exhibits the upper resonant hardening branch. A similar bifurcation pattern is found when $\gamma = 0.8$ (saddle-node bifurcations at L and M). On decreasing the frequency, the symmetric upper resonant solution undergoes a pitchfork bifurcation at N where it becomes

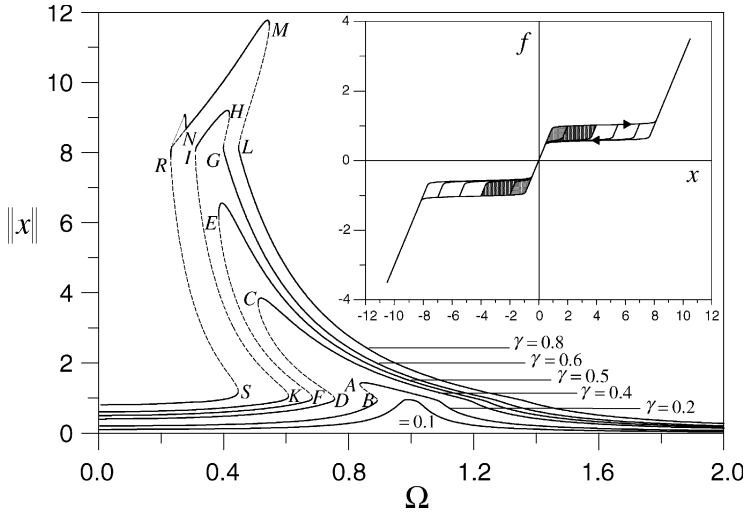

Fig. 6. Frequency–response curves in isothermal conditions when $q_1 = 1.05$ and $q_3 = 0.60$.

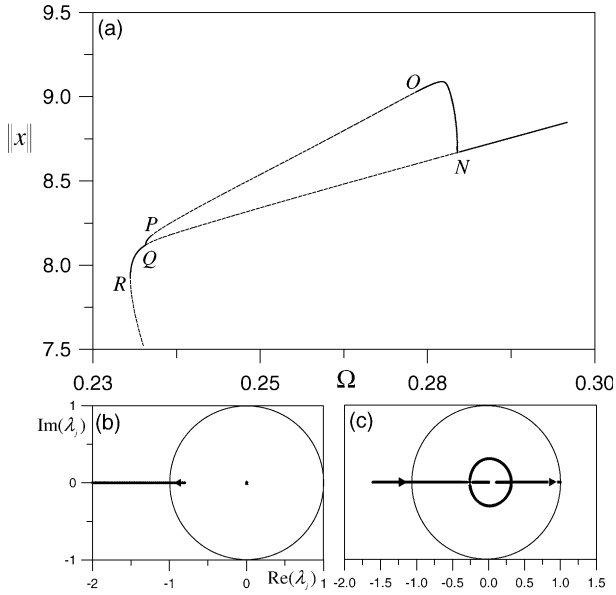

Fig. 7. (a) Enlargement of the frequency–response curve when $q_1 = 1.05$, $q_3 = 0.60$, and $\gamma = 0.8$. Variation of the Floquet multipliers in the complex plane near (b) the bifurcation point P and (c) the bifurcation points O and N.

unstable until Q (Fig. 7a) where it regains its stability by a reverse pitchfork bifurcation. The stable symmetric solution experiences a saddle-node bifurcation at R, slightly below Q. The resonant unstable symmetric solution and the nonresonant symmetric solution merge (Fig. 6) at the saddle-node bifurcation at S.

The scenario past the pitchfork bifurcation at N is discussed in finer details in Fig. 7. As shown in Fig. 7a, the newly born nonsymmetric solution is stable until O where it loses its stability via a period-doubling bifurcation. The nonsymmetric solution remains unstable until P where it regains its stability by a reverse period-doubling bifurcation. In Fig. 7b–c, the paths of the real and imaginary parts of the three Floquet multipliers for the nonsymmetric orbit are shown. These paths are constructed, for convenience, when the frequency is increased above Q (pitchfork bifurcation). As clear in Fig. 7b, one of the Floquet multipliers crosses the unit circle along the real axis through -1 at P (Figs. 7a and b). Thereafter, with further increase of the excitation frequency, one of the Floquet multipliers enters the unit circle (Fig. 7c) at O along the real axis through -1 (i.e., the unstable nonsymmetric solution regains its stability via a reverse period-doubling bifurcation). Eventually, one of the Floquet multipliers hits the unit circle at $+1$ on the real axis at the frequency corresponding to N (pitchfork bifurcation).

To investigate the scenario past the period-doubling bifurcations at O and P, numerical construction of the bifurcation diagrams, via direct integration of the governing equations, is necessary since the successive bifurcations are likely to be packed into smaller and smaller frequency ranges. The bifurcation diagrams in the frequency range $[0.2306, 0.2850]$ have been accordingly obtained by integrating (15), (16), and (21) over 1000 excitation cycles and collecting the points of the Poincaré map (the last 64 cycles) at each frequency as shown in Fig. 8. The system response exhibits a full bubble structure culminating into chaos. Interestingly, this bubble structure is remarkedly unsymmetrical with a clear period-doubling cascade in the right portion of the bubble. On the other hand, the structure of the period-doubling cascade is less discernible in the left portion of the bubble because it is localized in a smaller frequency range. In addition, it is worth noting the presence of boundary crises (with consequent enlargement of the chaotic attractor) and also the

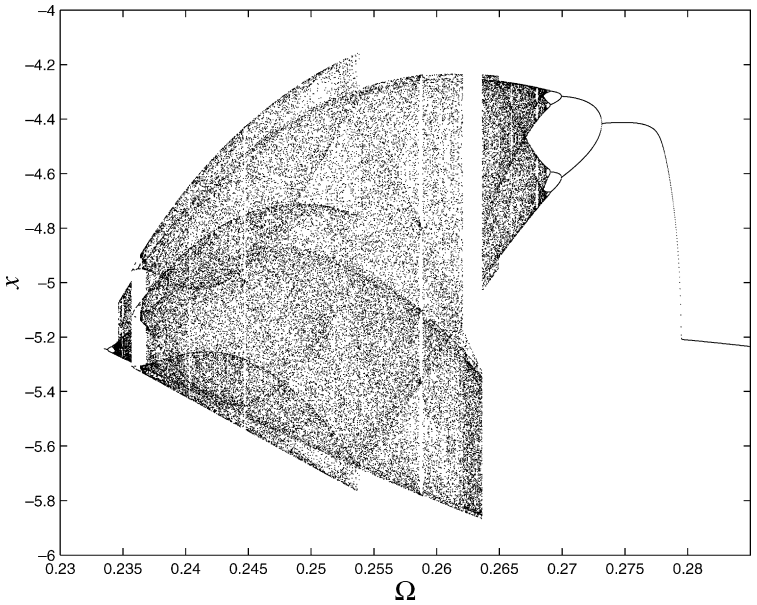

Fig. 8. Bifurcation diagram when $q_1 = 1.05$, $q_3 = 0.60$, and $\gamma = 0.8$.

appearance of embedded cascades of period doublings apparently involving a period-three solution likely born via a fold bifurcation. Further, periodic windows of different periodicity, mostly of period five, are noticed in agreement with similar observed period-doubling routes to chaos (Nayfeh and Balachandran, 1994).

To show some representative responses in the nonperiodic regime, two types of chaotic attractors are shown in Fig. 9. The signatures of the motions are outlined in the time histories of the displacement, the projections of the state orbit onto the (x, v)—(phase portraits) and (x, f)—plane (f is the pseudoelastic restoring force in the device), the Poincaré maps of x and v and the FFT's of the displacement. In Figs. 9a–d, the nonperiodic response when $\Omega = 0.2354$ is shown: a thin layer-structured strange attractor in the Poincaré map and the broadening of the frequency spectrum around some frequency components (subharmonics born out of successive period-doublings) can be observed. When $\Omega = 0.2551$ (Fig. 9e–h), the chaotic nature of the response is enhanced. This motion is located in the right portion of the bubble structure. Comparing Figs. 9b and f, it is clear that, in the latter case, the orbit visits larger regions of the state space and the associated FFT shows accordingly a broader frequency content.

As clear in the frequency–response curves in Fig. 6, the superharmonic resonances are activated for high excitation amplitudes. The frequency–response curve for $\gamma = 1$ is constructed and the superharmonic branch only is reported in Fig. 10. Decreasing the frequency past the saddle-node bifurcation at T, the amplitude of the stable symmetric response increases on the resonant branch (superharmonic resonance of order three) until U where it loses its stability via a supercritical pitchfork bifurcation. The stability is regained at Z via a reverse pitchfork bifurcation. Investigating the response within this range, it turns out that the nonsymmetric solution born at U becomes unstable and then stable again via period-doubling bifurcations at V and W, and X and Y, respectively. Past the reverse pitchfork bifurcation at Z, the solution reaches its peak amplitude and then experiences saddle-node bifurcations at a and b. Past b, the system undergoes superharmonic resonances of higher order. The superharmonic resonance of order five exhibits a multivalued range due to the saddle-node bifurcations at c and d; moreover, the subsequent superharmonic branch possesses an unstable region due to pitchfork bifurcations at e and f.

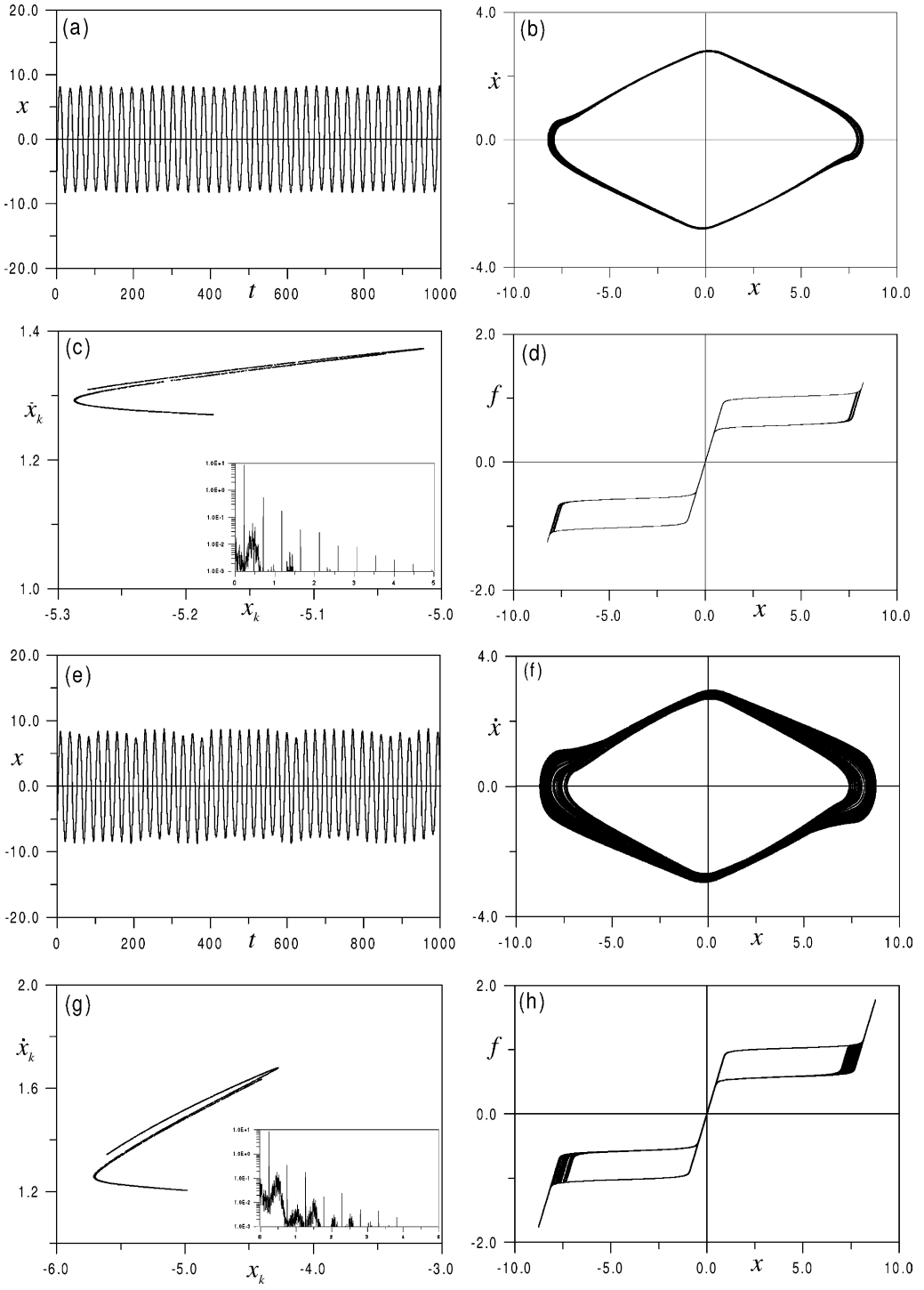

Fig. 9. Pseudoelastic responses when $q_1 = 1.05$, $q_3 = 0.60$, and $\gamma = 0.8$: (a) and (e) time histories of the displacement; (b) and (f) phase portraits; (c) and (g) Poincaré maps and superimposed FFT's of the displacement; (d) and (h) hysteresis loops of the restoring force when $\Omega = 0.2354$ (a)–(d) and $\Omega = 0.2551$ (e)–(h), respectively.

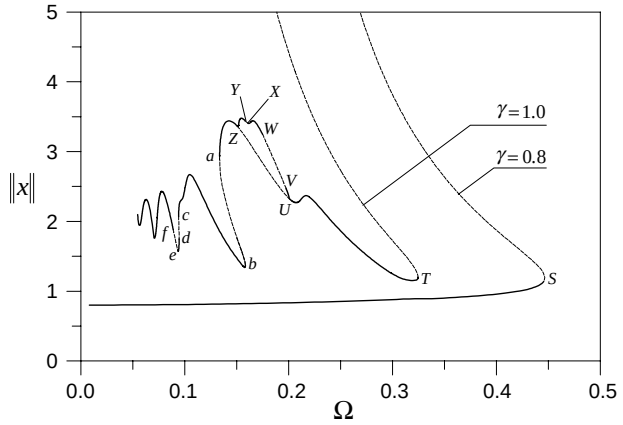

Fig. 10. Frequency–response curves in the superharmonic resonance range (isothermal conditions) when $q_1 = 1.05$ and $q_3 = 0.60$.

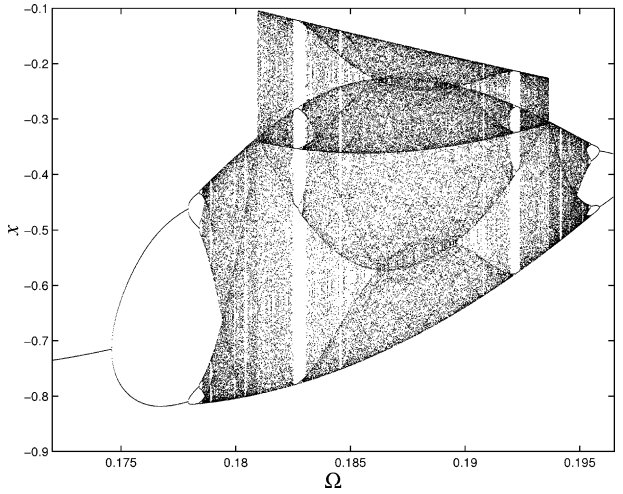

Fig. 11. Bifurcation diagram in the superharmonic resonance range when $q_1 = 1.05$ and $q_3 = 0.60$, and $\gamma = 1$.

The numerically constructed bifurcation diagram in the unstable region between U and Z (Fig. 11) confirms the predicted pitchfork and period-doubling bifurcations. More interestingly, in the region between the period-doubling bifurcations at V and W, a full bubble structure culminating into chaos is found. Within this complete bubble, boundary crises occur with consequent enlargement of the chaotic attractor, then fold bifurcations leading to period-five solutions are also to be noticed along with subsequent period-doubling cascades.

Chaotic responses emerging out of the superharmonic resonance are illustrated in Fig. 12 using the time history of the displacement, its FFT, the phase portrait, and the hysteresis loops. It is worth remarking that the amplitude of these chaotic responses is around 3, hence they are physically more realistic than the chaotic responses occurring in the primary-resonance frequency range. Furthermore, the chaoticity of the responses is more pronounced as clear in the time history, the FFT, and the hysteresis loops.

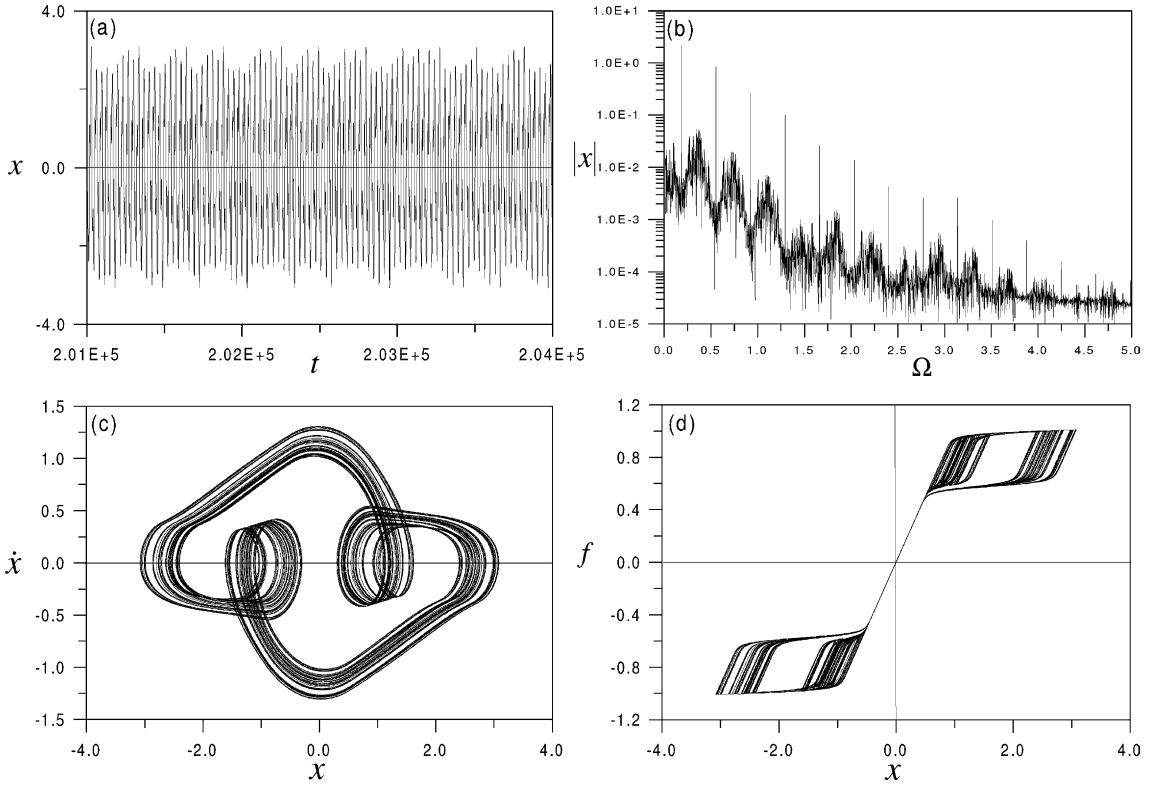

Fig. 12. Pseudoelastic response when $q_1 = 1.05$, $q_3 = 0.60$, $\gamma = 1.0$, and $\Omega = 0.18473$: (a) time history of the displacement; (b) FFT of the displacement; (c) phase portrait and (d) hysteresis loops of the restoring force.

5. Nonisothermal regime

As mentioned in Section 1, shape-memory devices interact thermodynamically with the external environment so that nonisothermal conditions may occur. These materials, contrary to traditional materials, under dynamic loading exhibit strong thermomechanical coupling with an ensuing influence on the mechanical response and bifurcation behavior as shown in this section.

In the following investigations, two nonisothermal regimes are considered, (i) typical operating conditions with the nondimensional heat exchange coefficient $h = 0.08$ and (ii) nearly adiabatic conditions with a relatively low value of h, $h = 0.001$.

The equations governing the dynamics of the system including the thermodynamics are given by the full set in Eqs. (15)–(18), including the temperature as a state variable. Therefore, the Poincaré map is four-dimensional, the monodromy matrix is 4×4 and four Floquet multipliers need to be monitored for ascertaining the stability and bifurcations.

The typical case ($h = 0.08$) is discussed first. In Fig. 13, the frequency–response curves of the maximum displacement (top) and maximum temperature (bottom) are shown. The same parameters as in the last isothermal case (nearly flat pseudoelastic plateau and thin hysteresis loops) are considered. However, three additional parameters are to be specified, namely L, J, and h; they are set to typical values for a pseudoelastic device in a convective environment, $L = 0.124$, $J = 0.315$, and $h = 0.08$. Concerning the nondimensional temperature scale, it is worth recalling that the dimensional temperature is expressed in Kelvin

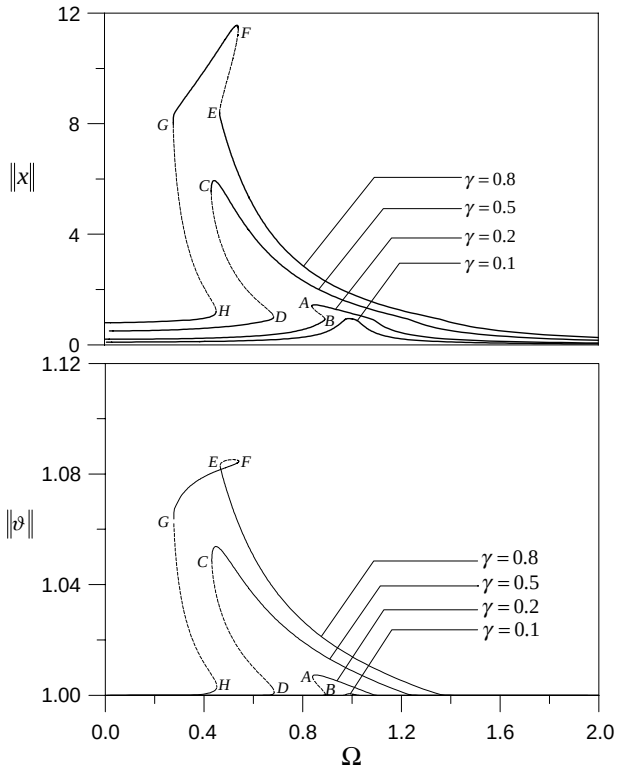

Fig. 13. Frequency–response curves in nonisothermal conditions when $q_1 = 1.05$, $q_3 = 0.60$, $J = 0.315$, $h = 0.08$, $\theta_E = 1.0$ and $L = 0.124$.

(K); when, for example, the environmental temperature is 20 °C (293 K), then a relatively small increase of the nondimensional temperature of 5% (i.e., $\theta = 1.05$) corresponds to a temperature variation of about 73% in Centigrade degrees.

The overall structure of the frequency–response curves with the associated bifurcations in the nonisothermal case is globally similar to the isothermal case (Fig. 6) but with some notable differences. When $\gamma = 0.8$, superharmonic resonances are not activated and the responses are always periodic. To clarify the thermomechanical behavior, it is worth pointing out that the temperature variations during oscillations are affected by two parameters: the amount of phase fraction transformed during the cycle (related to the maximum displacement) and the loading rate (related to the oscillation frequency); in particular, temperature variations increase with the maximum displacement and with the oscillation frequency. Obviously, within the range of maximum displacements less than one, no phase transformations occur; the behavior is linearly elastic and the device remains at the environment temperature. However, decreasing the excitation frequency from frequencies above the natural frequency, the maximum displacement amplitude increases along the resonant branch—due to the softening nature of the restoring force—and the temperature increases indicating clearly that the effect of the overall transformation amount overcomes that associated with the loading rate (frequency). This occurs because the maximum displacement increases more than proportionally with the frequency.

On the contrary, along the upper resonant branch (GF), the maximum temperature of the device increases with the frequency. Since on this branch $x > x_{Mf}$, the responses experience complete phase transformation cycles, hence the maximum displacement (transformation amount) does not exert any influence

and the temperature variations are now regulated exclusively by the loading rate. However, the corresponding unstable solutions (branch EF), although characterized by the same transformed amount and frequency, exhibit a higher temperature variation. These unstable solutions, as clear in Fig. 13 (top), have smaller maximum amplitudes than the stable ones, hence they differ for the extent of the excursion into the elastic range above x_{Mf}. Since during elastic loading and unloadings the heat is exchanged with the environment without any heat production, the solution with greater maximum displacement (stable solution) can exchange with the environment more heat than the unstable solution, hence it is characterized by a lower maximum temperature.

To show the signatures of some typical thermomechanical resonant responses, in Fig. 14, two coexisting resonant solutions are presented when $\gamma = 0.8$ and $\omega = 0.5388$. Figs. 14a–d show the response on the upper resonant hardening branch whereas Figs. 14e–h show that located on the lower branch. Inspecting the time histories of the displacement and temperature and the associated FFT's, it is worth noting, in agreement with Bernardini and Vestroni (2003), that the period of the temperature is one-half the period of the displacement as expected, according to the dependence of the phase-transformation heat production term, Z_2, in Eqs. (17) and (18), on the absolute value of the displacement. Physically, this implies that, in two complete phase transformation cycles ($\mathrm{A} \to \mathrm{M} \to \mathrm{A} \to \mathrm{M}$), one in tension and one in compression, the displacement goes through one complete cycle. Furthermore, there are higher-order harmonics contributing to the temperature evolution contrary to the displacement; this explains the slow convergence of semi-analytical methods such as the method of harmonic balance in nonisothermal conditions as observed in Bernardini and Vestroni (2003) where 12 harmonic components were used to achieve convergence. Clearly, the higher-order harmonics are more important in the upper resonant response (Fig. 14c) than in the lower one (Fig. 14g). In the former case, the response becomes elastic again above the displacement threshold x_{Mf} (Fig. 14d) and, during these excursions into the elastic range, the device releases heat into the surrounding environment. As a result, its temperature decreases exponentially although it seems to be a linear decay from the flat roofs in the temperature time history due to the small time window (about one-fourth the displacement period).

The superharmonic resonance has also been investigated considering an high excitation amplitude, $\gamma = 1$. As shown in Fig. 15, a number of superharmonic resonances are activated at this forcing level although, as expected, the superharmonic resonance of order one-third is the strongest. Within this resonance, there is a multi-valued range between the two saddle-node bifurcations L and M. Moreover, a small unstable range has been detected between J and K due to pitchfork bifurcations. Numerical inspection of this unstable range has not shown the existence of strange attractors. It can be concluded, from the comparison with the isothermal regime, that the thermomechanical coupling exerts, within the investigated range, a regularizing effect on the responses, likely due to the increased apparent stiffness resulting from the effect of the temperature on the transformation forces.

Next, the results relating to the nearly adiabatic case are illustrated. The frequency–response curves for the displacement and the temperature are shown in Fig. 16. It is clear that the thermodynamical coupling strongly modifies the system response to harmonic excitations. The frequency–response curves are certainly of the softening type, however, the bending is significantly reduced by the increased apparent stiffness due to the high temperature variations that occur as a consequence of the inhibited heat exchanges with the environment. Furthermore, the upper resonant hardening branches do not exist and there are no saddle-node bifurcations in the overall frequency range. In fact, as a result of the drastically reduced bending of the resonance curves, they do not exhibit vertical tangency points.

Instead of saddle-node bifurcations, above a threshold excitation amplitude (between 0.1 and 0.2), the periodic responses lose their stability at an excitation frequency below the linear natural frequency via a secondary Hopf bifurcation (also known as Neimark bifurcation) denoted with H_1. In Fig. 17, the paths of the four Floquet multipliers are shown when the excitation frequency is decreased. At H_1, a pair of complex conjugate multipliers intersect transversely the unit circle. Past the Hopf bifurcation, the two multipliers

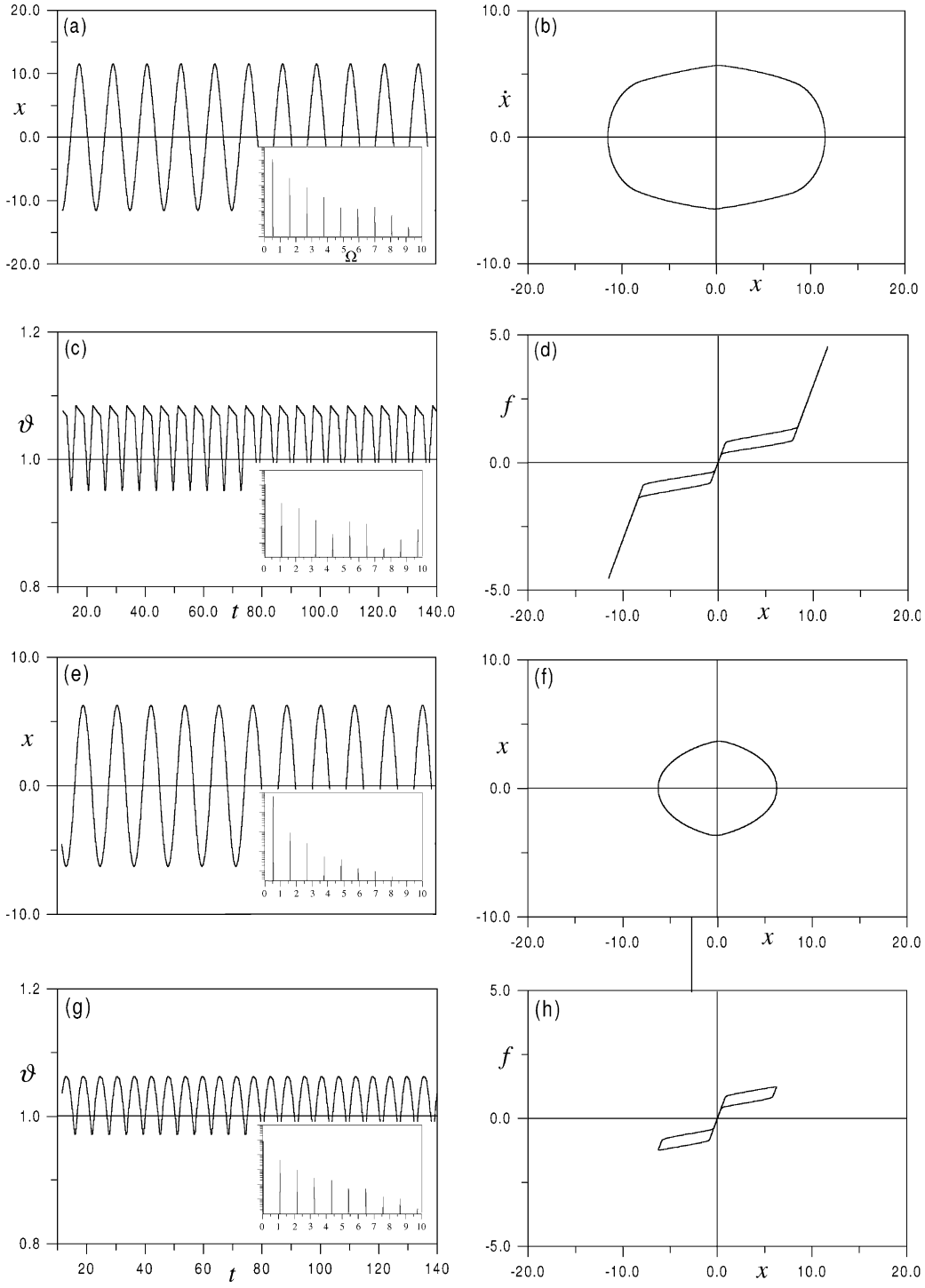

Fig. 14. Two coexisting stable responses ((a)–(d) upper resonant solution and (e)–(h) lower resonant solution) when $q_1 = 1.05$, $q_3 = 0.60$, $J = 0.315$, $h = 0.08$, $\theta_E = 1.0$, $L = 0.124$, $\gamma = 0.8$, and $\Omega = 0.5388$: (a) and (e) time histories of the displacement; (c) and (g) time histories of the temperature; (b) and (f) phase portraits; and (d) and (h) hysteresis loops.

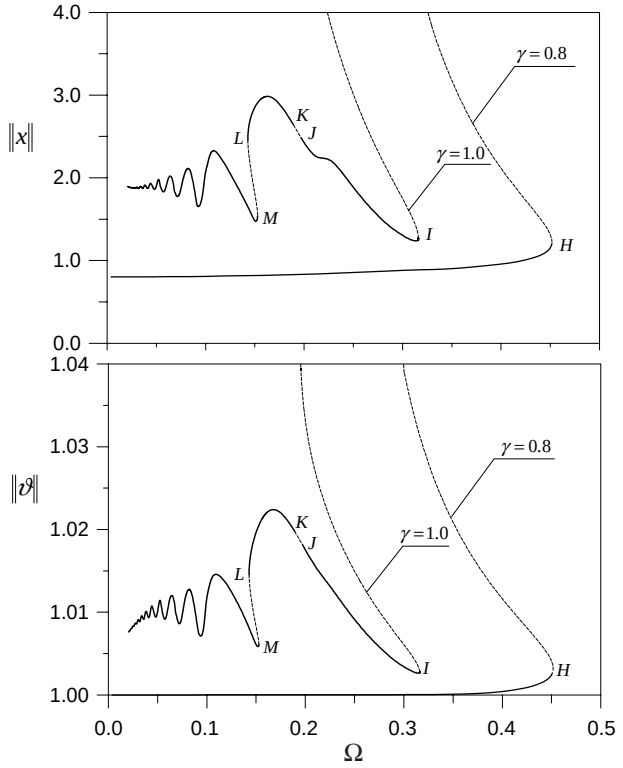

Fig. 15. Frequency–response curves in nonisothermal conditions in the superharmonic range when $q_1 = 1.05$, $q_3 = 0.60$, $J = 0.315$, $h = 0.08$, $\theta_E = 1.0$ and $L = 0.124$.

become real and move away from +1 in the positive real direction. At some intermediate value of the frequency in the range between H_1 and H_2 in Fig. 16, the multipliers direction is reversed and, as they approach the unit circle, they become complex conjugate. Hence, they re-enter the unit circle by transversal intersection at H_2. This is the reverse Hopf bifurcation similarly denoted in Figs. 16–18.

In the unstable regions between the Hopf bifurcations H_1 and H_2 in the frequency–response and frequency–temperature planes, respectively, indicated with a grey filling, the periodic solutions are unstable and quasiperiodic motions are born out of this dynamic instability. As in the previous case, the lower Hopf bifurcations occur at steady-state temperatures whose amplitudes are greater than the environmental temperature. We also note that, even for relatively low excitation amplitudes as 0.2–0.4, the maximum temperature variations are relatively high, above 100%. Of course, this outcome indicates that the use of such devices may become problematic when they are expected to operate in nearly adiabatic conditions because the extreme temperature variations may deteriorate or, in the limit, cause a breakdown of the devices.

The investigation of the unstable region between the Hopf bifurcations H_1 and H_2 is carried out constructing bifurcation diagrams via numerical integration of the governing equations. In Fig. 18, one of these bifurcation diagrams, in the frequency range [0.8–0.811] and for $\gamma = 0.4$ (relatively low excitation amplitude), is shown. At a first glance, the responses are neither periodic nor do they seem to be chaotic. A closer analysis of these responses, as it will be shown, has led to the conclusion that they are quasiperiodic, as expected past a Hopf bifurcation. The quasiperiodicity of these responses is, however, peculiar. Typically, past a Hopf bifurcation, a quasiperiodic response possesses two frequencies which are incommensurate,

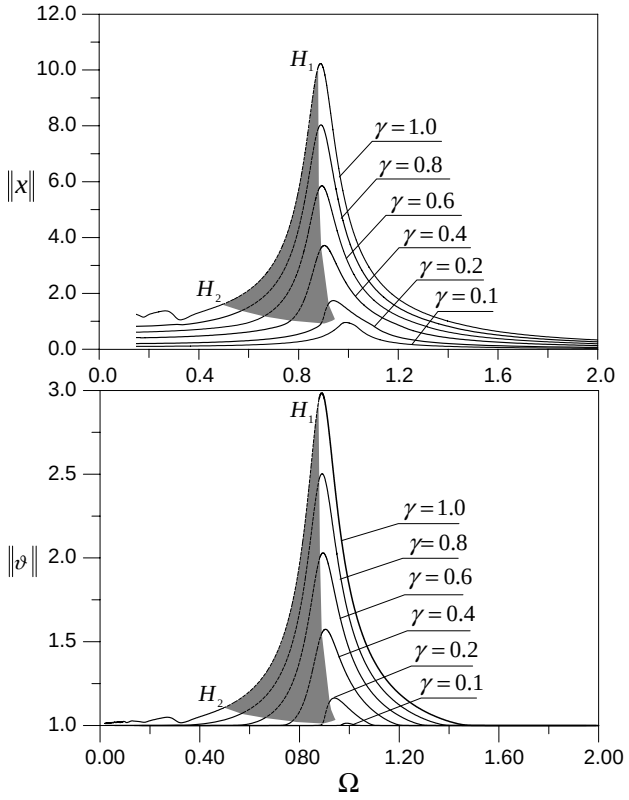

Fig. 16. Frequency–response curves in nonisothermal conditions when $q_1 = 1.05$, $q_3 = 0.60$, $J = 0.315$, $h = 0.001$, $\theta_E = 1.0$ and $L = 0.124$. The shaded region indicates the unstable solutions.

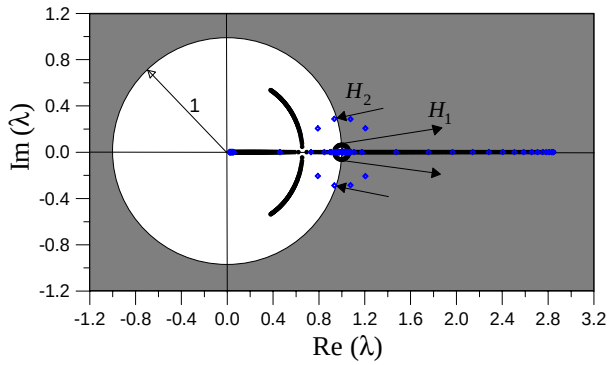

Fig. 17. Variation of the Floquet multipliers in the nonisothermal case near the Hopf bifurcations H_1 and H_2 when $q_1 = 1.05$, $q_3 = 0.60$, $J = 0.315$, $h = 0.001$, $\theta_E = 1.0$ and $L = 0.124$.

namely, the dominant excitation frequency (carrier frequency) and the Hopf-generated frequency. The motion is characterized by fast oscillations which are amplitude-modulated with the low frequency (modulation frequency). In Fig. 19, the time histories of the displacement, the temperature, and the entropy

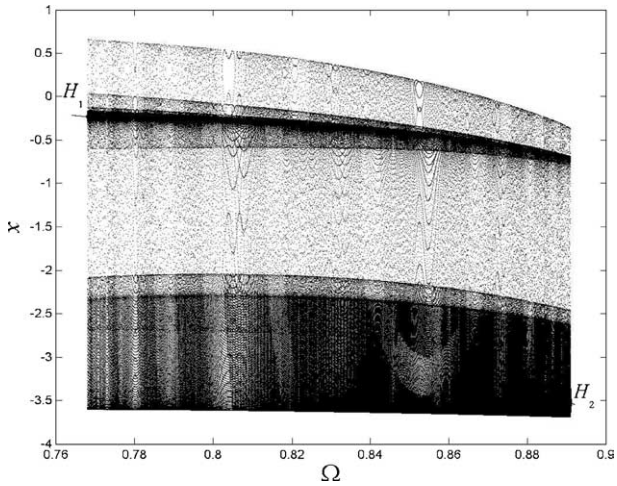

Fig. 18. Bifurcation diagram between H_1 and H_2 in nonisothermal conditions when $q_1 = 1.05$, $q_3 = 0.60$, $J = 0.315$, $h = 0.001$, $\theta_E = 1.0$, $L = 0.124$ and $\gamma = 0.40$.

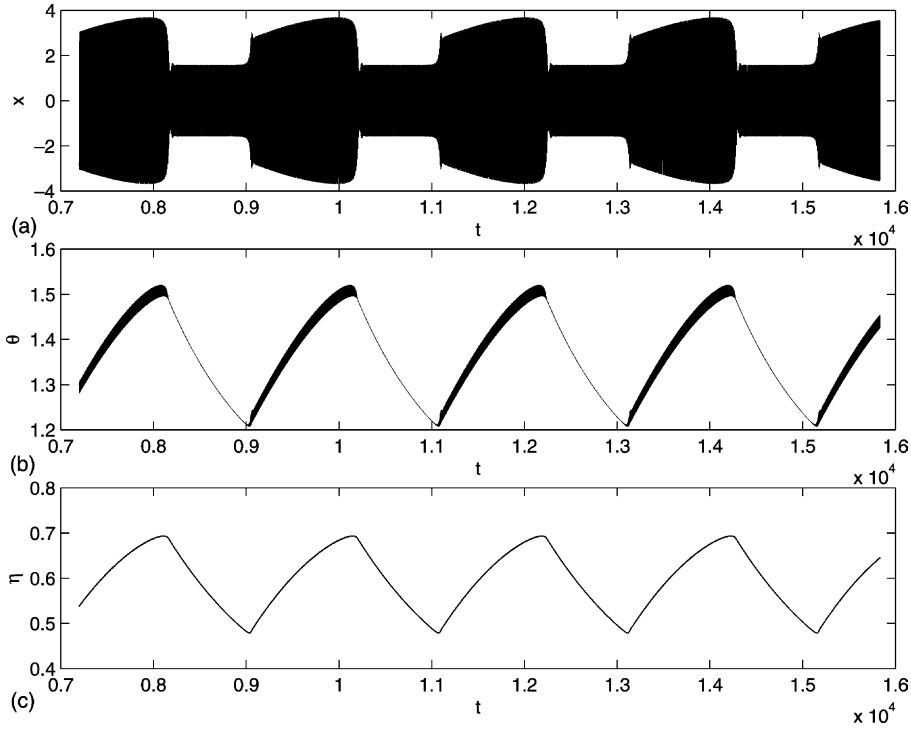

Fig. 19. Time histories of: (top) displacement; (middle) temperature and (bottom) entropy when $q_1 = 1.05$, $q_3 = 0.60$, $J = 0.315$, $h = 0.001$, $\theta_E = 1.0$, $L = 0.124$, $\gamma = 0.40$ and $\Omega = 0.87291$.

are shown when $\gamma = 0.4$ and $\Omega = 0.87291$. In this case (Fig. 19 top), the amplitude modulation shows a very long period. With an excitation period of 7.198, the period of the resulting motion is nearly 2093 with a

ratio of about 283 between the response period and the excitation period. Furthermore, the saw-tooth-like shape of the motion envelope suggests that the response must possess several harmonics which are multiple of the frequency component generated by the Hopf bifurcation. To corroborate this thinking, the FFT of the displacement has been computed and is shown in Fig. 20 where the presence of the carrier frequency ($\Omega = 0.87291$) and its odd integer multiples ($3\Omega, 5\Omega, 7\Omega, \ldots$, because the response is symmetric) are clear along with a wide number of almost indiscernible side bands around these frequencies. It turns out that, with a closer look at the FFT, there can be found a low-frequency component ($\approx 3.08 \times 10^{-3}$) and its integer multiples that create the side bands around the excitation frequency and its odd multiples in agreement with the previous qualitative analysis of the motion.

As far as the temperature is concerned, in Fig. 19, for half of its period, it undergoes an exponential-like decay and, for the other half, it grows exponentially with fast oscillations (at the excitation frequency) although with small amplitude. Interestingly, the entropy shows a clear low-frequency periodic motion without fast oscillations because both the temperature fluctuations and the phase transformations are too small.

To understand more closely the thermodynamical coupling mechanism responsible for these peculiar quasiperiodic responses, which are robust frequency- and amplitude-wise, the time histories of the displacement, the temperature, and the fraction of martensitic phase ξ along with the hysteresis loops in different time windows (marked with the letters a–d) are shown in Fig. 21. Before entering the time window (a), the amplitude of the oscillatory motion and that of the temperature are such that no phase transformations occur because the maximum force in one cycle is smaller than the transformation force, confirmed by the fact that $\xi = 0$ (Fig. 21), hence, no heat is generated by the device in this phase. Heat is, instead, released causing a temperature decrease. The temperature decay is exponential entailing that the rate of change of the temperature is mostly regulated by Newton's cooling law, Eq. (6). The characteristic time of this evolution is the inverse of the nondimensional heat exchange coefficient; that is, $T_c = h^{-1}$. It can be easily seen that the time length of this decay is of the order of the characteristic time.

The temperature decay continues until a temperature is reached whose associated transformation force equals the maximum force reached over one cycle. Therefore, phase transformations are initiated (i.e., $\xi > 0$) and, due to the generated heat, the temperature increases (time window (a)). The hysteresis loops grow in size at approximately the same transformation force. During this process, the phase transforma-

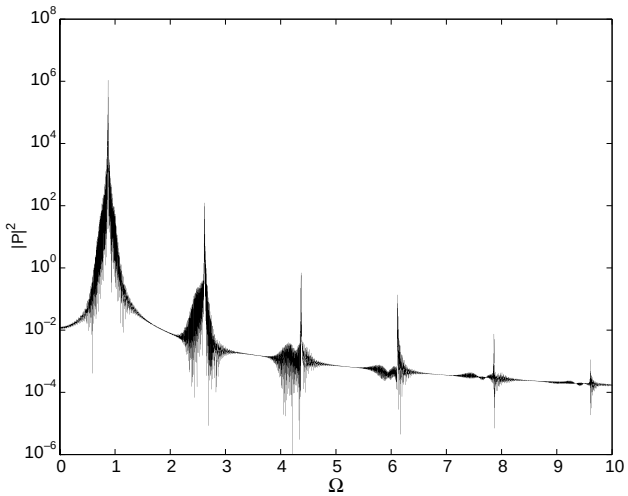

Fig. 20. FFT of the displacement when $q_1 = 1.05$, $q_3 = 0.60$, $J = 0.315$, $h = 0.001$, $\theta_E = 1.0$, $L = 0.124$, $\gamma = 0.40$ and $\Omega = 0.87291$.

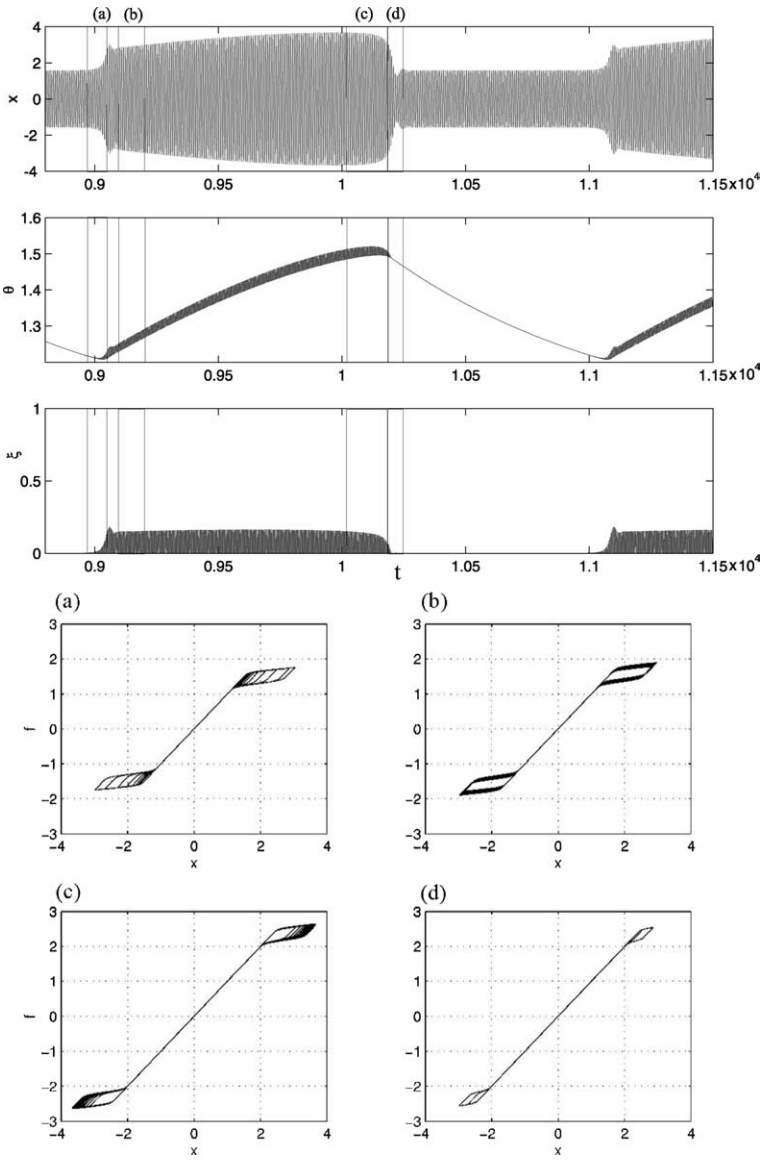

Fig. 21. Time histories of the displacement, the temperature and the Martensite fraction, and the hysteresis loops in time windows: (a)–(d) when $q_1 = 1.05$, $q_3 = 0.60$, $J = 0.315$, $h = 0.001$, $\theta_E = 1.0$, $L = 0.124$, $\gamma = 0.40$ and $\Omega = 0.87291$.

tions are clearly driving the mechanical variables because the increase in relative length of the device (resulting from the increasing phase transformations) makes the motion grow in amplitude (recall that the total displacement is considered).

In window (b), simultaneously with the growth of amplitude of the motion, the temperature continues to increase with an exponential-like envelope; consequently, the transformation force keeps increasing.

This process of growth of oscillation amplitude, temperature and transformation force (see time window (c) with the pseudoelastic plateaus clearly above 2) continues until the temperature is high enough such that the associated transformation force becomes higher than the current maximum force reached over one

cycle; hence, a rather fast decrease of phase transformation occurs and with it a rather sharp decrease of the oscillation amplitude follows. This process persists until no phase transformations occur at all and the system responds with low-amplitude elastic oscillations (time window (d)); subsequently, the motion replicates itself. The length of this growth is, again, of the order of the characteristic time. Hence, an estimate of the overall period is $2T_c = 2h^{-1}$ in agreement with the computed response period.

6. Conclusions

The nonlinear thermomechanical responses of shape-memory devices have been investigated employing a numerically accurate approach comprising a path-following scheme based on the Poincaré map method along with arclength parameterization. A model with internal variables has been used for the restoring force and the thermodynamical interactions between the device and the external environment have also been modeled employing the laws of thermodynamics and Newton's law of convection. The study has been specifically directed to outline the differences in the dynamical behaviors of shape-memory systems when they operate in isothermal conditions in contrast with more realistic nonisothermal conditions.

The responses to harmonic excitations are mainly periodic. Therefore, the behavior of the system is appropriately described by frequency–response curves constructed for various excitation levels and different device characteristics. Nonregular motions are investigated in the unstable regions of the fundamental periodic response. In the isothermal case, whereby the system does not experience temperature variations, the softening frequency–response curves possess a hardening branch above a threshold excitation level around the primary-resonance range. Furthermore, on this branch, for an excitation amplitude which is around 80% of the transformation force, a complete unsymmetrical bubble structure with a variety of chaotic responses and interposed high-periodicity motions is found to emerge out of pitchfork (symmetry breaking) and subsequent period-doubling bifurcations. Evidence of explosive bifurcations such as boundary crises and fold bifurcations has also been found. These phenomena are confined within a relatively narrow frequency range and occur at high amplitudes past the threshold value for complete phase transformations. On the other hand, around the superharmonic resonance of order three, complex dynamics with a bubble structure with complete period-doubling cascades occur. The chaotic responses in this region take place at an excitation amplitude around the transformation force threshold and are robust frequency-wise as they occur in a relatively large frequency band.

When the device exchanges heat with the environment, the system state variables are augmented with the temperature and the dynamic system becomes four-dimensional. The same class of shape-memory devices exhibiting complex dynamics in isothermal conditions has been investigated in the nonisothermal case. Two nonisothermal regimes have been explored depending on the nondimensional heat exchange coefficient: the case of ordinary operating conditions, when the heat is exchanged relatively fast, and a nearly adiabatic case, when the heat exchange is relatively slow. In the first case, within the considered excitation amplitudes, the dynamic behavior is somehow smoother than that in the corresponding isothermal conditions because the responses are always periodic and symmetric undergoing jumps only at the saddle-node bifurcations also in the superharmonic region. Therefore, the thermomechanical coupling under these conditions seems to act to destroy the bifurcations responsible for complex dynamic behaviors. Still, the SMM devices can respond with multiple attractors possessing different amplitudes but significantly different thermal states, and may switch from one attractor to the other under external perturbations.

In nearly adiabatic conditions, the thermodynamical coupling is such to profoundly modify the system behavior contrary to ordinary nonisothermal or isothermal conditions. First, the responses do not undergo jumps at all, are periodic and are stable in a relatively large frequency range. They experience Hopf bifurcations which give rise to peculiar quasiperiodic responses that turn out to be stable in a rather large frequency range. These quasiperiodic responses are intimately related to the thermodynamical coupling:

they are amplitude-modulated motions where the fundamental modulation period is very large and is shown to be of the order of the characteristic time regulating the mechanism of heat convection. Further, the distinguished character of the response frequency content is that, around the excitation frequency and its odd harmonics, a dense distribution of side bands is developed which makes the shape of the amplitude modulation quite complex. It is worth mentioning that nearly adiabatic conditions can be realized when the shape-memory devices are placed in housings where the heat exchange with the environment is relatively difficult.

As a result of the diverse and complex documented nonlinear phenomena occurring in nonisothermal conditions, it is clear that the thermodynamical coupling needs to be properly accounted for in modeling the dynamic behavior of shape-memory systems.

Acknowledgements

This work was partially supported by the FY-2001/02 MURST Grant COFIN'01 "Dynamics of Flexible Structures" and by the FY-2001 Grant *Giovani Ricercatori* (Young Investigators) "Theoretical and Experimental Investigations into the Dynamics of Intelligent Hysteretic Devices" sponsored by the University of Rome La Sapienza.

References

Bernardini, D., 2001. On the macroscopic free energy functions for shape memory alloys. Journal of the Mechanics and Physics of Solids 49, 813–837.

Bernardini, D., Pence, T.J., 2002. Shape memory materials: modeling. In: Encyclopedia of Smart Materials, 2. John Wiley and Sons, New York, pp. 972–983.

Bernardini, D., Vestroni, F., 2000. Hysteretic modeling of shape memory alloy vibration reduction devices. Journal of Material Production and Manufacturing Science 9, 101–112.

Bernardini, D., Vestroni, F., 2003. Non-isothermal oscillations of pseudoelastic devices. International Journal of Non-Linear Mechanics 38, 1297–1313.

Capecchi, D., Vestroni, F., 1990. Periodic response of a class of hysteretic oscillators. International Journal of Non-linear Mechanics 25, 309–317.

Clark, P.W., Aiken, I.D., Kelly, J.M., Higashino, M., Krumme, R., 1995. Experimental and analytical studies of SMA dampers for structural control. In: Proceedings of the Smart Structures and Material Conference 1995, San Diego, CA, 2445, pp. 241–251.

Coleman, B.D., Gurtin, M.E., 1967. Thermodynamics with internal state variables. Journal of Chemical Physics 47, 597–613.

Feng, Z.C., Li, D.Z., 1996. Dynamics of a mechanical system with a shape memory alloy bar. Journal of Intelligent Materials Systems and Structures 7, 399–410.

Ivshin, Y., Pence, T.J., 1994. A thermomechanical model for a one-variant shape memory material. Journal of Intelligent Materials Systems and Structures 5, 455–473.

Lacarbonara, W., Vestroni, F., 2003. Nonclassical responses of oscillators with hysteresis. Nonlinear Dynamics 32, 235–258.

Lacarbonara, W., Vestroni, F., Capecchi, D., 1999. Poincaré map-based continuation of periodic orbits in dynamic discontinuous and hysteretic systems, Paper No. DETC99/VIB-8088. In: Proceedings of the 17th Biennial ASME Conference on Mechanical Vibration and Noise, Las Vegas, NA, USA, September 12–15.

Lacarbonara, W., Bernardini, D., Vestroni, F., 2001. Periodic and nonperiodic responses of shape-memory oscillators, Paper No. DETC2001/VIB-21458. In: Proceedings of the 18th Biennial ASME Conference on Mechanical Vibration and Noise, Pittsburgh, PA, USA, September 9–12.

Masri, S.F., 1975. Forced vibration of the damped bilinear hysteretic oscillator. Journal of the Acoustical Society of America 57, 106–111.

Nayfeh, A.H., Balachandran, B., 1994. Applied Nonlinear Dynamics. Wiley-Interscience, New York.

Oberaigner, E.R., Tanaka, K., Fisher, F.D., 1995. Investigation of the damping behavior of a vibrating SMA rod. In: Proceedings of the Smart Structures and Materials Conference 1995, San Diego, CA, 2442, pp. 349–361.

Otsuka, K., Shimizu, K., 1986. Pseudoelasticity and shape memory effects in alloys. International Metals Reviews 31, 93–114.

Saadat, S., Salichs, J., Noori, M., Hou, Z., Davoodi, H., Bar-on, I., Suzuki, Y., Masuda, A., 2002. An overview of vibration and seismic applications of NiTi shape memory alloys. Smart Materials and Structures 11, 218–229.

Thomson, P., Balas, G.J., Leo, P.H., 1995. Pseudoelastic SMA models and effects on passive structural damping. In: Proceedings of the Smart Structures and Materials Conference 1995, San Diego, CA, 2445, pp. 188–199.

Vestroni, F., Bernardini, D., 1999. Nonlinear dynamic behavior of shape memory alloy oscillators. In: Kreuzer, E., Van Dao, N. (Eds.), Recent Developments in Nonlinear Oscillations of Mechanical Systems. Kluwer, The Netherlands, pp. 311–320.

Vestroni, F., Capecchi, D., 1997. Coupling and resonance phenomena in dynamic systems with hysteresis. In: Moon, F.C. (Ed.), Proceedings of the IUTAM Symposium on New Applications of Nonlinear and Chaotic Dynamics in Mechanics. Kluwer Academic Publishers, Dordrecht, pp. 203–212.

Wong, C.W., Ni, Y.Q., Lau, S.L., 1994a. Steady-state oscillation of hysteretic differential model. I: response analysis. ASCE Journal of Engineering Mechanics 120, 2271–2298.

Wong, C.W., Ni, Y.Q., Ko, J.M., 1994b. Steady-state oscillation of hysteretic differential model. II: performance analysis. ASCE Journal of Engineering Mechanics 120, 249–263.